further increases the clock-cycle time in MQCA devices by one or two orders of magnitude to eliminate precession from the switching process and to ensure predictable operation. Our simulations show that the majority gate reported here has an inherent operating speed of 100 MHz and dissipation below 1 eV per switching event. As a worst-case estimate of the power dissipation in an MQCA system, at these speeds, and assuming that all nanomagnets switch in each clock cycle, 10^{10} gates would dissipate ~0.1 W.

We performed Monte Carlo simulations in the single-domain approximation to investigate whether the realization of larger-scale systems is feasible (*24*). Variations in nanomagnet shape and edge roughness were taken into account in the distribution of the coupling fields at which switching occurs, i.e., switching fields (distribution of the demagnetization tensor elements), and thermal fluctuations were modeled by adding a stochastic field to the coupling field. We found that for our structures, the impact of switching-field variations is far more important than the effect of thermal fluctuations. Strongly coupled dots (<100-nm dot separation) fabricated by high-quality lithography (with switching-field variations less than 10%) exhibit magnetic ordering over 10 to 20 magnets. This result agrees well with our previous experiments (*25*, *26*) for samples fabricated by electron-beam lithography and lift-off (supporting online text). Even with better fabrication technology, the number of nanomagnets that can be clocked together is limited. Therefore, a larger-scale device would have to operate by means of local clocking of subarrays that realize a few gates only. The small number of magnets switching at the same time ensures that error levels can be kept acceptably small. This concept has been developed for EQCA (*27*). The most suitable architecture for adiabatically clocked MQCA devices appears to be a pipelined structure. Because of the sequential arrangement of logic gates, there will inevitably be pipeline latency; however, new data can be fed into the pipeline at each clock cycle. Clocking zones can be defined by locally applied clock-fields. Pipelined architectures are desirable in their own right owing to their highly parallelized computing environment.

Integration of MQCA elements with electronic circuitry is possible in a manner similar to that for magnetic random access memory (MRAM) elements (*28*). Furthermore, integration of MQCA arrays into MRAM cells is also feasible, thus allowing the possibility of "intelligent memory" whereby the magnetic layer of an MRAM cell could not only store a single bit of information, but could also perform basic logical processing. This may provide an opportunity to increase the functionality and integration density of an MRAM device.

In summary, MQCA information propagation and negation have been demonstrated previously (*2*, *25*, *26*), and our present work indicates that logic functions can also be realized in properly structured arrays of physically coupled nanomagnets. The technology for fabricating such nanometer-scale magnets is currently under development by the hard disk drive industry (*29*). Whereas the latter work focuses entirely on data-storage applications, and physical coupling between individual bits is undesirable, our work points out the possibility of also realizing logic functionality in such systems and indicates the potential of all-magnetic information-processing systems that incorporate both memory and logic.

References and Notes

1. A. Ney, C. Pampuch, R. Koch, K. H. Ploog, *Nature* **425**, 485 (2003).
2. R. P. Cowburn, M. E. Welland, *Science* **287**, 1466 (2000).
3. D. A. Allwood *et al.*, *Science* **296**, 2003 (2002).
4. D. A. Allwood *et al.*, *Science* **309**, 1688 (2005).
5. G. Csaba, A. Imre, G. H. Bernstein, W. Porod, V. Metlushko, *IEEE Trans. Nanotechnol.* **1**, 209 (2002).
6. C. S. Lent, P. D. Tougaw, W. Porod, G. H. Bernstein, *Nanotechnology* **4**, 49 (1993).
7. A. I. Csurgay, W. Porod, C. S. Lent, *IEEE Trans. Circ. Syst. I* **47**, 1212 (2000).
8. G. Csaba, A. I. Csurgay, W. Porod, *Int. J. Circ. Theory Appl.* **29**, 73 (2001).
9. G. Csaba, W. Porod, A. I. Csurgay, *Int. J. Circ. Theory Appl.* **31**, 67 (2003).
10. A. O. Orlov, I. Amlani, G. H. Bernstein, C. S. Lent, G. L. Snider, *Science* **277**, 928 (1997).
11. I. Amlani *et al.*, *Science* **284**, 289 (1999).
12. R. K. Kummamuru *et al.*, *IEEE Trans. Electron Devices* **50**, 1906 (2003).
13. A. O. Orlov *et al.*, *Mesoscopic Tunneling Devices*, H. Nakashima, Ed. (Research Signpost, Trivandrum, Kerala, India, 2004), p. 125.
14. G. L. Snider *et al.*, *J. Appl. Phys.* **85**, 4283 (1999).
15. C. S. Lent, *Science* **288**, 1597 (2000).
16. G. Csaba, W. Porod, *J. Comput. Electron.* **1**, 87 (2002).
17. M. C. B. Parish, M. Forshaw, *Appl. Phys. Lett.* **83**, 2046 (2003).
18. S. A. Haque, M. Yamamoto, R. Nakatani, Y. Endo, *J. Magn. Magn. Mater.* **282**, 380 (2004).
19. The micromagnetic simulations were performed using the Object Oriented Micromagnetic Framework (M. J. Donahue, D. G. Porter, OOMMF User's Guide, Version 1.0 Interagency Report NISTIR 6376, http://math.nist.gov/oommf/) of the National Institute of Standards and Technology.
20. The magnetizing process, i.e., the application of the clock-field, was performed in the homogeneous field of an electromagnet capable of a maximum 7000 Oe. Owing to limitations imposed by the ramping rate of the generated field, the frequency of the clock-field was about 0.01 Hz in our experiments.
21. Magnetic force microscopy images were taken in a Digital Instruments Nanoscope IV with standard magnetic probes.
22. Antiferromagnetic ordering was investigated in a large set of AFC lines designed to be identical. In a small percentage of results, we have found the ordering to fail even in the simplest, two-magnet systems. The identified faulty pairs performed highly repeatably, which indicates that the errors are related to fabrication variations (*30*).
23. Th. Gerrits, H. A. M. van den Berg, J. Hohlfeld, L. Bar, Th. Rasing, *Nature* **418**, 509 (2002).
24. G. Csaba, thesis, University of Notre Dame, IN (2003).
25. A. Imre, G. Csaba, G. H. Bernstein, W. Porod, V. Metlushko, *Proc. IEEE Nanotechnol.* **2**, 20 (2003).
26. A. Imre, G. Csaba, G. H. Bernstein, W. Porod, V. Metlushko, *Superlatt. Microstruct.* **34**, 513 (2003).
27. J. Timler, C. S. Lent, *J. Appl. Phys.* **91**, 823 (2002).
28. C. A. Ross, *Annu. Rev. Mater. Res.* **31**, 203 (2001).
29. J. M. Slaughter *et al.*, *J. Supercon.* **15**, 19 (2002).
30. G. H. Bernstein *et al.*, *Microelectr. J.* **36**, 619 (2005).

31. This work was supported in part by grants from the Office of Naval Research, the W. M. Keck Foundation, and the National Science Foundation.

Supporting Online Material

www.sciencemag.org/cgi/content/full/311/5758/205/DC1
SOM Text
References

23 September 2005; accepted 1 December 2005
10.1126/science.1120506

A Stretchable Form of Single-Crystal Silicon for High-Performance Electronics on Rubber Substrates

Dahl-Young Khang,[1,3,4] Hanqing Jiang,[2] Young Huang,[2]* John A. Rogers[1,2,3,4]*

We have produced a stretchable form of silicon that consists of submicrometer single-crystal elements structured into shapes with microscale, periodic, wavelike geometries. When supported by an elastomeric substrate, this "wavy" silicon can be reversibly stretched and compressed to large levels of strain without damaging the silicon. The amplitudes and periods of the waves change to accommodate these deformations, thereby avoiding substantial strains in the silicon itself. Dielectrics, patterns of dopants, electrodes, and other elements directly integrated with the silicon yield fully formed, high-performance "wavy" metal oxide semiconductor field-effect transistors, p-n diodes, and other devices for electronic circuits that can be stretched or compressed to similarly large levels of strain.

Progress in electronics is driven mainly by efforts to increase circuit operating speeds and integration densities, to reduce the power consumption of circuits, and, for display systems, to enable large area coverage. A more recent direction seeks to develop methods and materials that enable high-performance circuits to be formed on unconventional substrates with unusual form factors (*1*, *2*), such as flexible plastic substrates for

paperlike displays and optical scanners (*3*–*7*), spherically curved supports for focal plane arrays (*8*, *9*), and conformable skins for integrated robotic sensors (*10*, *11*). Many electronic materials can provide good bendability when prepared in thin-film form and placed on thin substrate sheets (*12*–*17*) or near neutral mechanical planes in substrate laminates (*18*, *19*). In these cases, the strains experienced by the active materials during bending can remain well below the typical levels required to induce fracture (~1%). Full stretchability, a much more challenging characteristic, is required for devices that can flex, stretch, or reach extreme levels of bending as they are operated or for those that can be conformally wrapped around supports with complex curvilinear shapes. In these systems, strains at the circuit level can exceed the fracture limits of nearly all known electronic materials, especially those that are well developed for established applications. This problem can be circumvented, to some extent, with circuits that use stretchable conducting wires to interconnect electronic components (such as transistors) supported by rigid isolated islands (*20*–*25*). Promising results can be obtained with this strategy, although it is best suited to applications that can be achieved with active electronics at relatively low coverages. We report a different approach, in which stretchability is achieved directly in thin films of high-quality, single-crystal Si that have micrometer-scale, periodic, "wave"-like geometries. These structures accommodate large compressive and tensile strains through changes in the wave amplitudes and wavelengths rather than through potentially destructive strains in the materials themselves. Integrating such stretchable wavy Si elements with dielectrics, patterns of dopants, and thin metal films leads to high-performance, stretchable electronic devices.

Figure 1 presents a fabrication sequence for wavy, single-crystal Si ribbons on elastomeric (rubber) substrates. The first step (top panel) involves photolithography to define a resist layer on a Si-on-insulator (SOI) wafer, followed by etching to remove the exposed parts of the top Si. Removing the resist with acetone and then etching the buried SiO_2 layer with concentrated hydrofluoric acid releases the ribbons from the underlying Si substrate. The ends of the ribbons connect to the wafer to prevent them from washing away in the etchant. The widths (5 to 50 μm) and lengths (~15 mm) of the resist lines define the dimensions of the ribbons. The thickness of the top Si (20 to 320 nm) on the SOI wafers defines the ribbon thicknesses. In the next step (middle panel), a flat elastomeric substrate [poly(dimethylsiloxane) (PDMS), 1 to 3 mm thick] is elastically stretched and then brought into conformal contact with the ribbons. Peeling the PDMS away lifts the ribbons off of the wafer and leaves them adhered to the PDMS surface. Releasing the strain in the PDMS (that is, the prestrain) leads to surface deformations that cause well-defined waves to form in the Si and the PDMS surface (Fig. 2, A and B). The relief profiles are sinusoidal (top panel, Fig. 2C), with periodicities between 5 and 50 μm and amplitudes between 100 nm and 1.5 μm, depending on the thickness of the Si and the level of prestrain in the PDMS. For a given system, the periods and amplitudes of the waves are uniform to within ~5% over large areas (several square centimeters). The flat morphology of the PDMS between the ribbons and the absence of correlated phases in waves of adjacent ribbons suggest that the ribbons are not strongly coupled mechanically. Figure 2C (bottom panel) shows micro-Raman measurements of the Si peak, measured as a function of distance along one of the wavy ribbons. The results provide insights into the stress distributions.

The behavior in this static wavy configuration is consistent with nonlinear analysis of the initial buckled geometry in a uniform, thin, high-modulus layer on a semi-infinite low-modulus support (*26*, *27*)

$$\lambda_0 = \frac{\pi h}{\sqrt{\varepsilon_c}},\ A_0 = h\sqrt{\frac{\varepsilon_{pre}}{\varepsilon_c} - 1} \qquad (1)$$

where $\varepsilon_c = 0.52\left[\frac{E_{PDMS}\left(1-\nu_{Si}^2\right)}{E_{Si}\left(1-\nu_{PDMS}^2\right)}\right]^{2/3}$ is the critical strain for buckling, ε_{pre} is the level of prestrain, λ_0 is the wavelength, and A_0 is the amplitude. The Poisson ratio is ν, the Young's modulus is E, and the subscripts refer to properties of the Si or PDMS. The thickness of the Si is h. This treatment captures many features of the as-fabricated wavy structures. Figure 2D shows, for example, that when the prestrain value is fixed (~0.9% for these data), the wavelengths and amplitudes both depend linearly on the Si thickness. The wavelengths do not depend on the level of prestrain (fig. S1). Furthermore, calculations that use literature values (*28*, *29*) for the mechanical properties of the Si and PDMS (E_{Si} = 130 GPa, E_{PDMS} = 2 MPa, ν_{Si} = 0.27, ν_{PDMS} = 0.48) yield amplitudes and wavelengths that are within ~10% (maximum deviation) of the measured values. The strains computed from the ratio of the effective lengths of the ribbons (as determined from the wavelength) to their actual lengths [as determined from surface distances measured by atomic force microscopy (AFM)], which we refer to as ribbon strains, yield values that are approximately equal to the prestrain in the PDMS, for prestrains up to ~3.5%. The peak (that is, the maximum) strains in the Si itself, which we refer to as Si strains, can be estimated from the ribbon thicknesses and radii of curvature at the extrema of the waves according to $\kappa h/2$, where κ is the curvature, in regimes of strain where the waves exist and where the critical strain (~0.03% for the cases examined here) is small as compared to the peak strains associated with bending. For the data of Fig. 2, the peak Si strains are ~0.36 (±0.08)%, which is more than a factor of 2 smaller than the ribbon strains. This Si

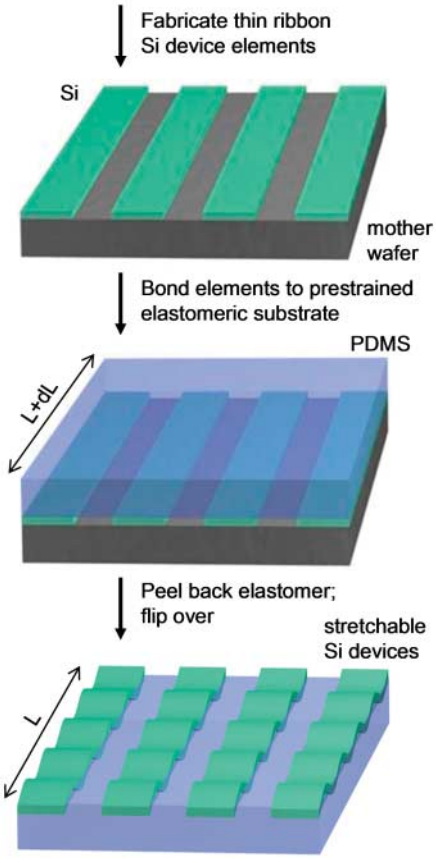

Fig. 1. Schematic illustration of the process for building stretchable single-crystal Si devices on elastomeric substrates. The first step (**top**) involves fabrication of thin (thicknesses between 20 and 320 nm) elements of single-crystal Si or complete integrated devices (transistors, diodes, etc.) by conventional lithographic processing, followed by etching of the top Si and SiO_2 layers of a SOI wafer. After these procedures, the ribbon structures are supported by, but not bonded to, the underlying wafer. Contacting a prestrained elastomeric substrate (PDMS) to the ribbons leads to bonding between these materials (**middle**). Peeling back the PDMS, with the ribbons bonded on its surface, and then releasing the prestrain, causes the PDMS to relax back to its unstrained state. This relaxation leads to the spontaneous formation of well-controlled, highly periodic, stretchable wavy structures in the ribbons (**bottom**).

[1]Department of Materials Science and Engineering, [2]Department of Mechanical and Industrial Engineering, [3]Beckman Institute for Advanced Science and Technology, [4]Seitz Materials Research Laboratory, University of Illinois, Urbana-Champaign, Urbana, IL 61801, USA.

*To whom correspondence should be addressed. E-mail: jrogers@uiuc.edu (J.A.R); huang9@uiuc.edu (Y.H.)

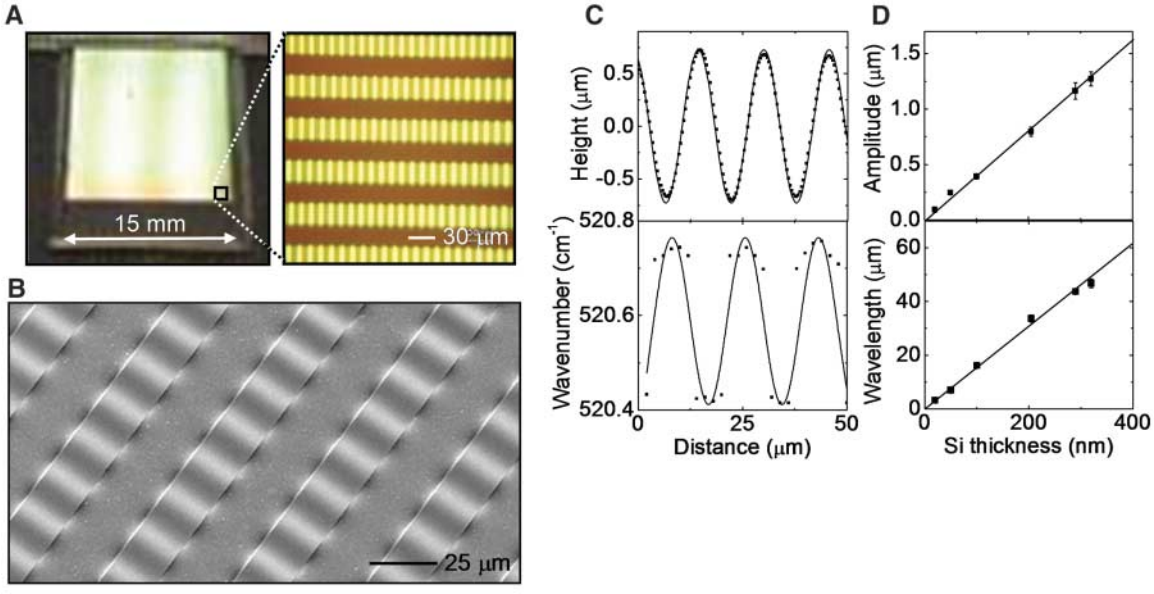

Fig. 2. (**A**) Optical images of a large-scale aligned array of wavy, single-crystal Si ribbons (widths = 20 μm, spacings = 20 μm, thicknesses = 100 nm) on PDMS. (**B**) Angled-view scanning electron micrograph of four wavy Si ribbons from the array shown in (A). The wavelengths and amplitudes of the wave structures are highly uniform across the array. (**C**) Surface height (top panel) and wavenumber of the Si Raman peak (bottom panel) as a function of position along a wavy Si ribbon on PDMS, measured by AFM and Raman microscopy, respectively. The lines represent sinusoidal fits to the data. (**D**) Amplitudes (top panel) and wavelengths (bottom panel) of wavy Si ribbons as a function of the thickness of the Si, all for a given level of prestrain in the PDMS. The lines correspond to calculations, without any fitting parameters.

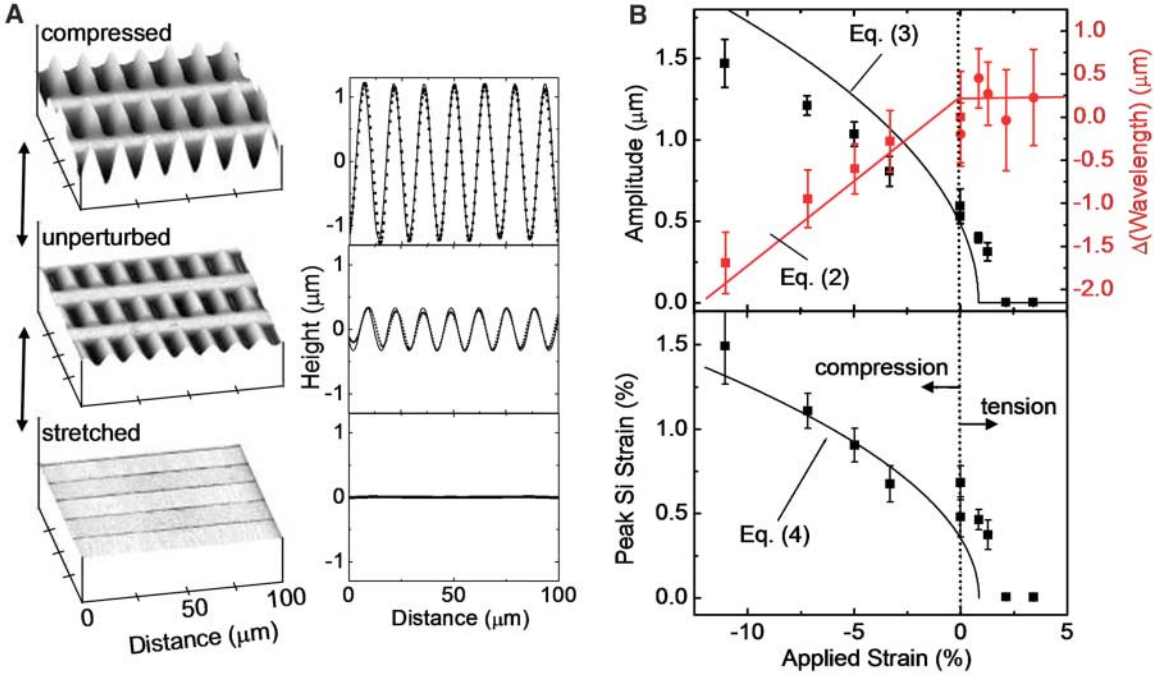

Fig. 3. (**A**) Atomic force micrographs (left panels) and relief profiles (right panels; the lines are the sinusoidal fits to experimental data) of wavy single-crystal Si ribbons (width = 20 μm, thickness = 100 nm) on PDMS substrates. The top, middle, and bottom panels correspond to configurations when the PDMS is strained along the ribbon lengths by −7% (compression), 0% (unperturbed), and 4.7% (stretching), respectively, measured at slightly different locations. (**B**) Average amplitudes (black) and changes in wavelength (red) of wavy Si ribbons as a function of strain applied to the PDMS substrate (top panel). For the wavelength measurements, different substrates were used for tension (circles) and compression (squares). Peak Si strains as a function of applied strain are shown in the bottom panel. The lines in these graphs represent calculations, without any free fitting parameters.

strain is the same for all ribbon thicknesses, for a given prestrain (fig. S2). The resulting mechanical advantage, in which the peak Si strain is substantially less than the ribbon strain, is critically important for achieving stretchability. Buckled thin films have also been observed in metals and dielectrics evaporated or spin-cast onto PDMS (in contrast to preformed, transferred, single-crystal elements and devices, as described here) (*30*–*32*).

The dynamic response of the wavy structures to compressive and tensile strains applied to the elastomeric substrate after fabrication is of primary importance for stretchable electronic devices. To reveal the mechanics of this process, we measured the geometries of wavy Si ribbons by AFM as force was applied to the PDMS to compress or stretch it parallel to the long dimension of the ribbons. This force creates strains both along the ribbons and perpendicular to them, due to the Poisson effect. The perpendicular strains lead primarily to deformations of the PDMS in the regions between the ribbons. The strains along the ribbons, on the other hand, are accommodated by changes in the structure of the waves. The three-dimensional height images and surface profiles in Fig. 3A present representative compressed, unperturbed, and stretched states (collected from slightly different locations on the sample). In these and other cases, the ribbons maintain their sinusoidal (lines in the right-hand panels of Fig.

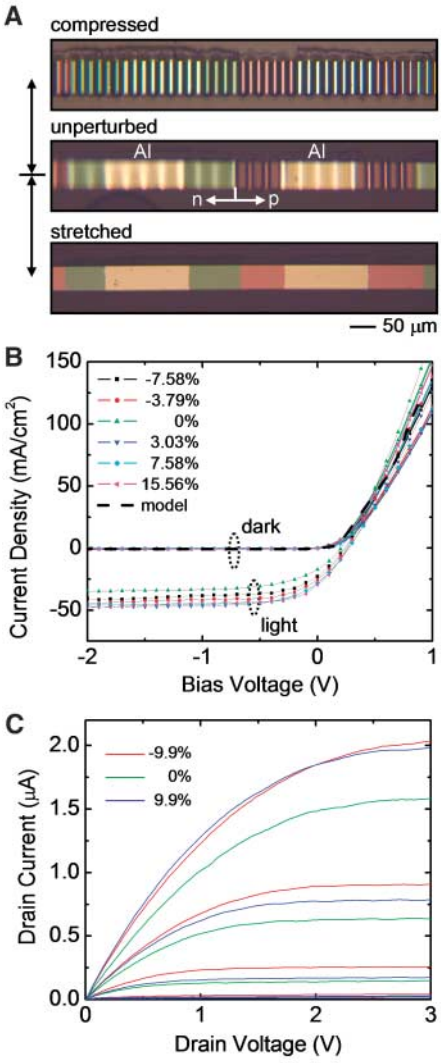

Fig. 4. (**A**) Optical images of a stretchable single-crystal Si p-n diode on a PDMS substrate at –11% (top), 0% (middle), and 11% (bottom) applied strains. The Al regions correspond to thin (20 nm) Al electrodes; the pink and green regions correspond to n (boron)– and p (phosphorous)–doped areas of the Si. (**B**) Current density as a function of bias voltage for stretchable Si p-n diodes, measured at various levels of applied strain. The curves labeled "light" and "dark" correspond to devices exposed to or shielded from ambient light, respectively. The solid curves show modeling results. (**C**) Current-voltage characteristics of a stretchable Schottky-barrier Si MOSFET, measured at –9.9%, 0%, and 9.9% applied strains (the gate voltage varied from 0 V to –5 V, with a 1-V step).

3A) shapes during deformation, in which approximately half of the wave structure lies beneath the unperturbed position of the PDMS surface, as defined by the regions between the ribbons (fig. S3). Figure 3B shows the wavelength and amplitude for compressive (negative) and tensile (positive) applied strains relative to the unperturbed state (zero). The data correspond to averaged AFM measurements collected from a large number (>50) of ribbons per point. The applied strains were determined from the measured end-to-end dimensional changes of the PDMS substrate. Direct surface measurements by AFM, as well as contour integrals evaluated from the sinusoidal wave shapes, show that the applied strains are equal to the ribbons strains (fig. S4) for the cases examined here. [The small-amplitude (<5 nm) waves that persist at tensile strains larger than the prestrain minus the critical strain might result from slight slippage of the Si during the initial buckling process. The computed peak Si strains and ribbon strains in this small- (or zero-) amplitude regime underestimate the actual values.] The results indicate two physically different responses of the wavy ribbons to applied strain. In tension, the waves evolve in a non-intuitive way: The wavelength does not change appreciably with applied strain, which is consistent with post-buckling mechanics. Instead, changes in amplitude accommodate the strain. In this regime, the Si strain decreases as the PDMS is stretched; it reaches ~0% when the applied strain equals the prestrain. By contrast, in compression, the wavelengths decrease and amplitudes increase with increasing applied strain. This mechanical response is similar to that of an accordion bellows, which is qualitatively different than the behavior in tension. During compression, the Si strain increases with the applied strain, due to the decreasing radii of curvature at the wave peaks and troughs. The rates of increase and magnitudes of the Si strains are, however, both much lower than the ribbon strains, as shown in Fig. 3B. These mechanics enable stretchability.

The full response in regimes of strain consistent with the wavy geometries can be quantitatively described by equations that give the dependence of the wavelength λ on its value in the initial buckled state, λ_0, and the applied strain $\varepsilon_{applied}$ according to

$$\lambda = \begin{cases} \lambda_0 & \text{for tension} \\ \lambda_0(1+\varepsilon_{applied}) & \text{for compression} \end{cases} \quad (2)$$

This tension/compression asymmetry can arise, for example, from slight reversible separations between the PDMS and the raised regions of Si, formed during compression. For this case, as well as for systems that do not exhibit this asymmetric behavior, the wave amplitude A, for both tension and compression, is given by a single expression, valid for modest strains (<10 to 15%) (*33*)

$$A = \sqrt{A_0^2 - h^2\frac{\varepsilon_{applied}}{\varepsilon_c}} = h\sqrt{\frac{\varepsilon_{pre}-\varepsilon_{applied}}{\varepsilon_c} - 1} \quad (3)$$

where A_0 is the value corresponding to the initial buckled state. These expressions yield quantitative agreement with the experiments without any parameter fitting, as shown in Fig. 3A. When the waviness, which accommodates the tensile/compressive strains, remains, the peak Si strain is dominated by the bending term and is given by (*33*)

$$\varepsilon_{Si}^{peak} = 2\varepsilon_c\sqrt{\frac{\varepsilon_{pre}-\varepsilon_{applied}}{\varepsilon_c} - 1} \quad (4)$$

which agrees well with the strain measured from curvature in Fig. 3B (see also fig. S5). Such an analytic expression is useful to define the range of applied strain that the system can sustain without fracturing the Si. For a prestrain of 0.9%, this range is –27% to 2.9% if we assume that the Si failure strain is ~2% (for either compression or tension). Controlling the level of prestrain allows this range of strains (that is, nearly 30%) to balance desired degrees of compressive and tensile deformability. For example, a prestrain of 3.5% (the maximum that we examined) yields a range of –24% to 5.5%. Such calculations assume that the applied strain equals the ribbon strain, even at extreme levels of deformation. Experimentally, we find that these estimates are often exceeded because of the ability of the PDMS beyond the ends of the ribbons and between the ribbons to accommodate strains, so that the applied strain is not completely transferred to the ribbons.

We have created functional, stretchable devices by including at the beginning of the fabrication sequence (Fig. 1, top panel) additional steps to define patterns of dopants in the Si, thin metal contacts, and dielectric layers using conventional processing techniques (*33*). Two- and three-terminal devices, diodes, and transistors, respectively, fabricated in this manner provide basic building blocks for circuits with advanced functionality. A dual transfer process in which the integrated ribbon devices were first lifted off of the SOI onto an undeformed PDMS slab, and then to a prestrained PDMS substrate, created wavy devices with metal contacts exposed for probing. Figure 4, A and B, show optical images and electrical responses of a stretchable p-n–junction diode for various levels of strain applied to the PDMS. We observed no systematic variation in the electrical properties of the devices when stretched or compressed, to within the scatter of the data. (The deviation in the curves is due mainly to variations in the quality of probe contacts.) As expected, these p-n–junction diodes can be used as photodetectors (at reverse-biased state) or as photovoltaic devices, in addition to their use as normal rectifying devices. The photocurrent density was ~35 mA/cm² at a reverse bias voltage of ~–1V. At forward bias, the short-circuit current density and open-circuit voltage were ~17 mA/cm² and 0.2 V, respectively, which yields a fill factor of 0.3. The shape of the response is consistent with modeling (solid curves in Fig. 4B). The device properties do not change substantially, even after

~100 cycles of compressing, stretching, and releasing (fig. S6). Figure 4C shows current-voltage characteristics of a stretchable, wavy, Si, Schottky-barrier metal oxide semiconductor field-effect transistor (MOSFET) formed with procedures similar to those used for the p-n diode, and with an integrated thin layer (40 nm) of thermal SiO_2 as a gate dielectric (*33*). The device parameters extracted from electrical measurements of this wavy transistor [linear regime mobility ~100 cm^2/Vs (likely contact-limited), threshold voltage ~–3 V] are comparable to those of devices formed on the SOI wafers under the same processing conditions (figs. S7 and S8). As with the p-n diodes, these wavy transistors can be reversibly stretched and compressed to large levels of strain without damaging the devices or substantially altering their electrical properties. In both the diodes and the transistors, deformations in the PDMS beyond the ends of the devices lead to device (ribbon) strains that are smaller than the applied strains. The overall stretchability results from the combined effects of device stretchability and these types of PDMS deformations. At compressive strains larger than those examined here, the PDMS tended to bend in ways that made probing difficult. At larger tensile strains, the ribbons either fractured, or slipped and remained intact, depending on the Si thickness, the ribbon lengths, and the strength of bonding between the Si and PDMS.

These stretchable Si MOSFETs and p-n diodes represent only two of the many classes of wavy electronic devices that can be formed. Completed circuit sheets or thin Si plates can also be structured into uniaxial or biaxial stretchable wavy geometries. Besides the unique mechanical characteristics of wavy devices, the coupling of strain to electronic properties, which occurs in many semiconductors, might provide opportunities to design device structures that exploit mechanically tunable periodic variations in strain to achieve unusual electronic responses. These and other areas appear promising for future research.

References and Notes

1. S. R. Forrest, *Nature* **428**, 911 (2004).
2. For recent progress and reviews, see *Proc. IEEE* **93**, issues 7 and 8 (2005).
3. J. A. Rogers *et al.*, *Proc. Natl. Acad. Sci. U.S.A.* **98**, 4835 (2001).
4. H. O. Jacobs, A. R. Tao, A. Schwartz, D. H. Gracias, G. M. Whitesides, *Science* **296**, 323 (2002).
5. H. E. A. Huitema *et al.*, *Nature* **414**, 599 (2001).
6. C. D. Sheraw *et al.*, *Appl. Phys. Lett.* **80**, 1088 (2002).
7. Y. Chen *et al.*, *Nature* **423**, 136 (2003).
8. H. C. Jin, J. R. Abelson, M. K. Erhardt, R. G. Nuzzo, *J. Vac. Sci. Technol. B* **22**, 2548 (2004).
9. P. H. I. Hsu *et al.*, *IEEE Trans. Electron. Devices* **51**, 371 (2004).
10. T. Someya *et al.*, *Proc. Natl. Acad. Sci. U.S.A.* **101**, 9966 (2004).
11. H. C. Lim *et al.*, *Sens. Act. A* **119**, 332 (2005).
12. J. Vandeputte *et al.*, U.S. Patent 6,580,151 (2003).
13. T. Sekitani *et al.*, *Appl. Phys. Lett.* **86**, 073511 (2005).
14. E. Menard, R. G. Nuzzo, J. A. Rogers, *Appl. Phys. Lett.* **86**, 093507 (2005).
15. H. Gleskova *et al.*, *J. Noncryst. Solids* **338**, 732 (2004).
16. S.-H. Hur, O. O. Park, J. A. Rogers, *Appl. Phys. Lett.* **86**, 243502 (2005).
17. X. F. Duan *et al.*, *Nature* **425**, 274 (2003).
18. Z. Suo, E. Y. Ma, H. Gleskova, S. Wagner, *Appl. Phys. Lett.* **74**, 1177 (1999).
19. Y.-L. Loo *et al.*, *Proc. Natl. Acad. Sci. U.S.A.* **99**, 10252 (2002).
20. T. Someya *et al.*, *Proc. Natl. Acad. Sci. U.S.A.* **102**, 12321 (2005).
21. S. P. Lacour, J. Jones, S. Wagner, Z. G. Suo, *Proc. IEEE* **93**, 1459 (2005).
22. S. P. Lacour *et al.*, *Appl. Phys. Lett.* **82**, 2404 (2003).
23. D. S. Gray, J. Tien, C. S. Chen, *Adv. Mater.* **16**, 393 (2004).
24. R. Faez, W. A. Gazotti, M. A. De Paoli, *Polymer* **40**, 5497 (1999).
25. C. A. Marquette, L. J. Blum, *Biosens. Bioelectron.* **20**, 197 (2004).
26. X. Chen, J. W. Hutchinson, *J. Appl. Mech.* **71**, 597 (2004).
27. Z. Y. Huang, W. Hong, Z. Suo, *J. Mech. Phys. Solids* **53**, 2101 (2005).
28. *Properties of Silicon* (INSPEC, Institution of Electrical Engineers, New York, 1988).
29. A. Bietsch, B. Michel, *J. Appl. Phys.* **88**, 4310 (2000).
30. N. Bowden *et al.*, *Nature* **146**, 146 (1998).
31. W. T. S. Huck *et al.*, *Langmuir* **16**, 3497 (2000).
32. C. M. Stafford *et al.*, *Nat. Mater.* **3**, 545 (2004).
33. Materials and methods are available as supporting material on *Science* Online.

34. We thank T. Banks for help with processing using the facilities at the Frederick Seitz Materials Research Laboratory. This work was supported by the Defense Advanced Research Projects Agency–funded Air Force Research Laboratory–managed Macroelectronics Program Contract FA8650-04-C-7101, by the U.S. Department of Energy under grant DEFG02-91-ER45439, and by NSF under grant DMI-0328162.

Supporting Online Material

www.sciencemag.org/cgi/content/full/1121401/DC1
Materials and Methods
Figs. S1 to S8

17 October 2005; accepted 5 December 2005
Published online 15 December 2005;
10.1126/science.1121401
Include this information when citing this paper.

Grain Boundary Strengthening in Alumina by Rare Earth Impurities

J. P. Buban,[1] K. Matsunaga,[1]* J. Chen,[2] N. Shibata,[1] W. Y. Ching,[2] T. Yamamoto,[3] Y. Ikuhara[1]†

Impurity doping often alters or improves the properties of materials. In alumina, grain boundaries play a key role in deformation mechanisms, particularly in the phenomenon of grain boundary sliding during creep at high temperatures. We elucidated the atomic-scale structure in alumina grain boundaries and its relationship to the suppression of creep upon doping with yttrium by using atomic resolution microscopy and high-precision calculations. We find that the yttrium segregates to very localized regions along the grain boundary and alters the local bonding environment, thereby strengthening the boundary against mechanical creep.

Structural ceramics have a large range of applications for engines and turbines. To avoid failure, the material needs to have a high resistance to deformations at the very high operating temperatures. Deformations almost always nucleate at atomic-scale defects, particularly grain boundaries (GBs). A commonly used and well-studied structural ceramic is alumina (Al_2O_3). However, GBs in Al_2O_3 are known for having a weak resistance to deformations via sliding because of creep (*1*–*5*) at high temperatures. One method to improve the resistance to sliding due to creep is through the addition of small amounts of rare earth elements (*4*, *5*). These additives (i.e., dopants) are known to segregate to the GBs and are expected to retard GB sliding. Systematic measurements of GB sliding by creep tests were investigated by using a pair of bicrystals (*6*). One was pristine and the other was Y-doped, with a tilt angle about the [0001] axis of ~18°, corresponding to a Σ value of 31 (*7*). Here, the Σ value represents the degree of geometrical coincidence at GB. These results showed that Y doping increased the creep resistance for even a single GB by two orders of magnitude. Several simple models to explain the increase in GB creep resistance due to rare earth impurity doping have been proposed (*4*, *5*), but the atomic-scale mechanism of how these dopants actually strengthen grain boundaries is still very unclear and controversial. This is mainly because of poor understanding of the atomic structure of alumina GBs and how it is affected by rare earth doping.

We describe the results of our investigation of the atomic mechanism of Y doping and of the increase in grain boundary mechanical strength with the use of *Z*-contrast

[1]Institute of Engineering Innovation, University of Tokyo, 2-11-16, Yayoi, Bunkyo, Tokyo 113–8656, Japan. [2]Department of Physics, University of Missouri–Kansas City, 5100 Rockhill Road, Kansas City, MO 64110–2499, USA. [3]Department of Advanced Materials Science, University of Tokyo, 5-1-5, Kashiwanoha, Kashiwa, Chiba 277–8561, Japan.

*Present address: Department of Materials Science and Engineering, Kyoto University, Yoshida-Honmachi, Sakyo, Kyoto 606–8501, Japan.

†To whom correspondence should be addressed. E-mail: ikuhara@sigma.t.u-tokyo.ac.jp